

[robotics.sciencemag.org/cgi/content/full/6/53/eabf5116/DC1](https://robotics.sciencemag.org/cgi/content/full/6/53/eabf5116/DC1)

## Supplementary Materials for

### **Robotic surfaces with reversible, spatiotemporal control for shape morphing and object manipulation**

Ke Liu, Felix Hacker, Chiara Daraio\*

\*Corresponding author. Email: [daraio@caltech.edu](mailto:daraio@caltech.edu)

Published 7 April 2021, *Sci. Robot.* **6**, eabf5116 (2021)  
DOI: [10.1126/scirobotics.abf5116](https://doi.org/10.1126/scirobotics.abf5116)

#### **The PDF file includes:**

- Note S1. Reduced-order model for numerical simulation.
- Note S2. Curvature estimation of a single composite beam.
- Fig. S1. Fabrication of the LCE strips.
- Fig. S2. Experimental setup for characterization of the actuation behavior of the LCE strips.
- Fig. S3. Mechanical testing of the LCE strips.
- Fig. S4. Characterization of the buckling and post-buckling behavior of the passive ribbons.
- Fig. S5. Derivation of the curvature of the composite beams.
- Fig. S6. Numerical demonstration of geometries obtained by controlling each LCE segment independently.
- Fig. S7. A robotic surface with denser mesh grid transforms into various shapes.
- Fig. S8. Fabrication of the heating coils.
- Fig. S9. The reduced-order model for simplified simulation of the robotic surface.
- References (58–60)

#### **Other Supplementary Material for this manuscript includes the following:**

(available at [robotics.sciencemag.org/cgi/content/full/6/53/eabf5116/DC1](https://robotics.sciencemag.org/cgi/content/full/6/53/eabf5116/DC1))

- Movie S1 (.mp4). Continuous shape morphing of the robotic surface.
- Movie S2 (.mp4). Object manipulation.
- Movie S3 (.mp4). Weight lifting.
- Movie S4 (.mp4). Numerical simulations using the reduced-order model.

## Note S1. Reduced-order model for numerical simulation.

The schematic diagram of the reduced order model used for our simulations is shown in Fig. S9A. Denoting the displacements of nodes in the reduced order model as  $\mathbf{u}$ , the system's total energy can be calculated as:

$$\Pi(\mathbf{u}) = E_S(\mathbf{u}) + E_A(\mathbf{u}) + E_R(\mathbf{u}). \quad (\text{S1})$$

Here,  $E_S$  is the elastic energy stored in the bar elements (i.e., in the extensional springs), which are used to model the passive ribbons subjected to in-plane stretching.  $E_A$  is the energy stored in the tension-only bar elements, which are used to model the LCE strips. Finally,  $E_R$  is the elastic energy stored in the torsional springs, which are used to model the out-of-plane bending of the passive ribbons. Equilibrium is achieved when:

$$\frac{\partial \Pi}{\partial \mathbf{u}} = \frac{\partial E_S}{\partial \mathbf{u}} + \frac{\partial E_A}{\partial \mathbf{u}} + \frac{\partial E_R}{\partial \mathbf{u}} = \mathbf{0}. \quad (\text{S2})$$

Each term in the above equation represents the internal forces caused by deformation of the corresponding elements.

For the bar elements modeling in-plane stretching of the passive ribbons, we define the stored energy by specifying energy density per volume, denoted as  $\mathcal{W}_S$ . The principle stretch  $\lambda_1$  is defined as  $L/L_0$ , where  $L_0$  is the undeformed, rest length and  $L$  is the deformed length. We adopt a simple 2-term Ogden model (51)  $\mathcal{W}_S$  under uniaxial loading:

$$\mathcal{W}_S(\lambda_1) = \frac{E}{\alpha_1 - \alpha_2} \left( \frac{\lambda_1^{\alpha_1} - 1}{\alpha_1} + \frac{\lambda_1^{\alpha_2} - 1}{\alpha_2} \right). \quad (\text{S3})$$

Here,  $E$  is the tensile modulus of Kapton (2.5 GPa),  $\alpha_1$  and  $\alpha_2$  are material constants taken arbitrarily as 5 and 1, respectively. For small strains, this constitutive model approximates linear elastic behavior, which occurs in our simulations as the in-plane deformation of the passive ribbons is very small. Denoting  $\nu$  as the material's Poisson's ratio, to recover the in-plane

Poisson's effect, we define the member areas as (53):

$$A_w = t_p \frac{b^2 - \nu w^2}{2b(1 - \nu^2)}, \quad A_b = t_p \frac{w^2 - \nu b^2}{2w(1 - \nu^2)}, \quad A_d = t_p \frac{\nu(b^2 + w^2)^{3/2}}{2bw(1 - \nu^2)}. \quad (\text{S4})$$

Here,  $t_p$  demotes thickness of the ribbons,  $w$  and  $b$  are the sides of the discretized rectangles, and the subscript  $d$  refers to the diagonals (see Fig. S9A).

Similarly, for bar elements modeling the LCE strips, we define the energy density function  $\mathcal{W}_A$  as:

$$\mathcal{W}_A(\lambda_1) = \begin{cases} \sum_{p=1}^3 \frac{\mu_p}{\alpha_p} \left( \lambda_1^{\alpha_p} + 2\lambda_1^{-\alpha_p/2} \right), & \lambda_1 > 1, \\ 0, & \lambda_1 \leq 1, \end{cases} \quad (\text{S5})$$

which is a 3-term incompressible Ogden hyperelastic model under uniaxial loading modified for zero compression stiffness. The parameters are fitted from experimental data (see Fig. 2D):  $\mu_1 = 0.4183$ ,  $\alpha_1 = 6.1965$ ,  $\mu_2 = 0.8086$ ,  $\alpha_2 = 0.8382$ ,  $\mu_3 = -0.4900$ ,  $\alpha_3 = 5.9338$ . Because each LCE strip is modeled as two such bars, the cross-sectional area of each bar element is half of an LCE strip. As we take reference of deformation to the isotropic phase of the LCE material, the area is determined to be  $5 \text{ mm}^2$ . In the simulation, to model the contraction of the LCE strips, we gradually reduce  $L_0$  until designated length. At each step we reduced  $L_0$ , the measure of  $\lambda_1$  changes, and energy stored in the active bar elements increases, leading to unbalanced internal forces. A Newton-Raphson algorithm is adopted to iteratively find a new equilibrium configuration of the system, resolving the unbalanced forces induced by decrease of  $L_0$ .

After discretization of the passive ribbon, the angles between any pair of hinged triangles approximate bending deformations. The stored energy of each bending hinge is assumed to be a direct function of the hinge length  $L_h$  and rotation angle  $\beta$ , which is defined as:

$$\mathcal{H}(L_h, \beta) = \frac{1}{2} L_h K \beta^2, \quad (\text{S6})$$

where  $K$  denotes the rotational stiffness per unit length along the axis of rotation, and  $\beta$  is a function of nodal displacements  $\mathbf{u}$  (52). To determine  $K$ , we consider a beam with cross section

$t_p \cdot w$  under pure bending and neglecting in-plane deformation. The stored energy of the discrete system should be equal to the stored energy in the continuum system, and thus we have (see Fig. S9B):

$$\int_0^L \frac{EI}{2r^2} = \sum_{i=1}^{L/b} \frac{1}{2} w K \left( \frac{b}{r} \right)^2, \quad (\text{S7})$$

which leads to:

$$K = \frac{EI}{wb}, \quad (\text{S8})$$

where  $I = wt_p^3/12$ . This formula needs to be corrected because it is derived based on small strain theory and neglecting in-plane deformations. In addition, the discretization scheme also affects the  $K$  value. In the actual implementation of our reduced-order model, based on the experimental data, the value of  $K$  is assigned as:

$$K = \frac{5.5Et^3}{12b}, \quad (\text{S9})$$

which leads to the result shown in Fig. 2G when  $b = 1.8$  mm, and yields consistent behavior as  $b$  varies (see Fig. S9C).

To account for contact and prevent unrealistic penetration of the active bars with the passive ribbons, we introduce torsional springs between the virtual plane formed by the pairs of active bar elements and the passive ribbons (see Fig. S9A). These special torsional springs should have zero stiffness for most range of its rotation, but exhibit large resistance when penetration is about to happen. We adopt the following constitutive model to approximate the effect of physical contact:

$$M = \begin{cases} L_h \xi \tan \left( \frac{\pi(\varphi - \varphi_1)}{2\varphi_1} \right), & 0 < \varphi \leq \varphi_1, \\ 0, & \varphi > \varphi_1 \end{cases} \quad (\text{S10})$$

where  $M$  is the resistance moment of this special torsional spring, and  $\varphi_1 = 30^\circ$ , and the coefficient  $\xi$  is taken a small value as  $1 \times 10^{-5}$  so that these torsional springs do not significantly change the system energy until a penetration is about to happen. As a result,  $M$  approaches

infinity when  $\varphi$  is close to 0, that is when the active bars are about to penetrate the passive ribbons.

## Note S2. Curvature estimation of a single composite beam.

To derive the curvature of a single composite beam after actuation, we assume that the top and bottom LCE strips have a circular shape, as shown in Fig. S5A. Denoting the length of the LCE strips in the isotropic phase as  $\ell_I$ , and the effective thickness (distance between the mid-planes of the top and bottom LCE strips) as  $h$ , we obtain:

$$\ell_I \lambda_T - \ell_I \lambda_B = \tau \left( R + \frac{h}{2} \right) - \tau \left( R - \frac{h}{2} \right), \quad (\text{S11})$$

which leads to:

$$\tau = \frac{\ell_I(\lambda_T - \lambda_B)}{h}. \quad (\text{S12})$$

The curvature of the center line of the composite beam is then estimated as:

$$\kappa = \frac{1}{R} = \frac{2\tau}{\ell_I(\lambda_T + \lambda_B)} = \frac{2(\lambda_T - \lambda_B)}{h(\lambda_T + \lambda_B)}. \quad (\text{S13})$$

Next, we derive the expression for  $h$ . Because the passive ribbons are much thinner than the LCE strips, we may ignore their thickness in this derivation. As a result,  $h$  is the sum of one thickness of the LCE strip (denoted as  $t_a$ ) and the buckled height of the passive ribbon (denoted as  $h_b$ ), as shown in Fig. S5B. The buckled shape of each segment of the passive ribbon is solved as planar elastica (58-60). In our case, as the buckling amount remains relatively small, we may approximate the buckled shape of the passive ribbons as a trigonometric function, the leading term of the asymptotic expansion of the exact solution (60):

$$y = -\frac{h_b}{2} \cos \left( \frac{2\pi x}{\ell} \right). \quad (\text{S14})$$

The arclength of the buckled shape is then:

$$\ell_p = \int_0^\ell \sqrt{1 + \frac{h_b^2 \pi^2 \sin^2 \left( \frac{2\pi x}{\ell} \right)}{\ell^2}} dx, \quad (\text{S15})$$

which must be a constant that equals the straight length of the passive ribbon before buckling (denoted as  $\ell_p$ ). Our goal is to solve  $h$  given  $\ell$  and  $\ell_p$ . Equation (S15) is an incomplete elliptic integral of the second kind, which makes it difficult to solve inversely and obtain closed form expression for  $h$ . Hence, we take another approximation here:

$$h_b \approx \frac{\ell_p}{2} \sqrt{1 - \left(\frac{\ell}{\ell_p}\right)^2}. \quad (\text{S16})$$

The red curve in Fig. S5C shows a level set of  $\ell_p$  given  $\ell$  and  $h_b$ , while the approximation made by Eq. (S16) is plotted in blue. In our case, we are working with  $0.5 < \ell/\ell_p \leq 1$ . We can see that Eq. (S16) overestimates the value of  $h$  given  $\ell$  and  $\ell_p$ , but converges to the exact solution when  $\ell \rightarrow \ell_p$ . When the composite beam is curved, the top and bottom LCE strips have different lengths. So we use their average length to calculate the ratio  $\ell/\ell_p$ :

$$\frac{\ell}{\ell_p} = \frac{\lambda_T + \lambda_B}{2\lambda_N}. \quad (\text{S17})$$

We then obtain an approximation for  $h$  as:

$$h = t_a + h_b \approx t_a + \ell_p \sqrt{4 - \left(\frac{\lambda_T + \lambda_B}{\lambda_N}\right)^2}. \quad (\text{S18})$$

Now, substituting Eq. (S18) into Eq. (S13), we obtain:

$$\kappa \approx \frac{16(\lambda_T - \lambda_B)}{(\lambda_T + \lambda_B)(t_a + \ell_p \sqrt{4 - (\lambda_T + \lambda_B)^2 / \lambda_N^2})}. \quad (\text{S19})$$

Comparing with the experimental data, we find that the above formula overestimates the curvature obtained in experiment and the numerical simulation. To correct this overestimation, we correct Eq. (S19) with a linear adjusting parameter  $\eta$ . We end up with the following formula:

$$\kappa = \frac{16\eta(\lambda_T - \lambda_B)}{(\lambda_T + \lambda_B)(t_a + \ell_p \sqrt{4 - (\lambda_T + \lambda_B)^2 / \lambda_N^2})}. \quad (\text{S20})$$

Here,  $\eta = 0.57$  according to regression from the experimental data.

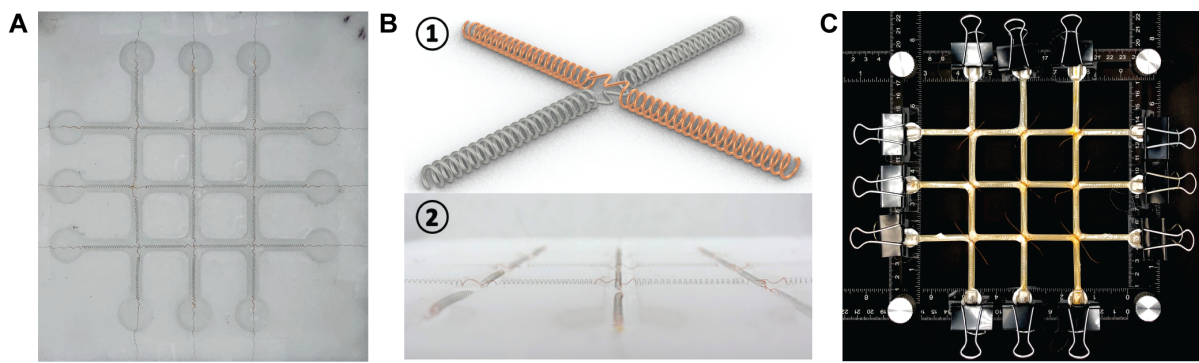


**Fig. S1. Fabrication of the LCE strips.** (A) The HDPE mold with grid shaped channel slots. The heating coils are placed in the slots. (B) Placement of the heating coil inside the mold. The top figure illustrates how the two crossing coils are separated at the joints. (C) The stretched grid of LCE strips before second-stage UV irradiation. We tie the LCE network onto a precursor network beneath it to obtain uniform stretch on all segments. The precursor network is cut from a Kapton film, similar in shape to the grid of passive ribbons.

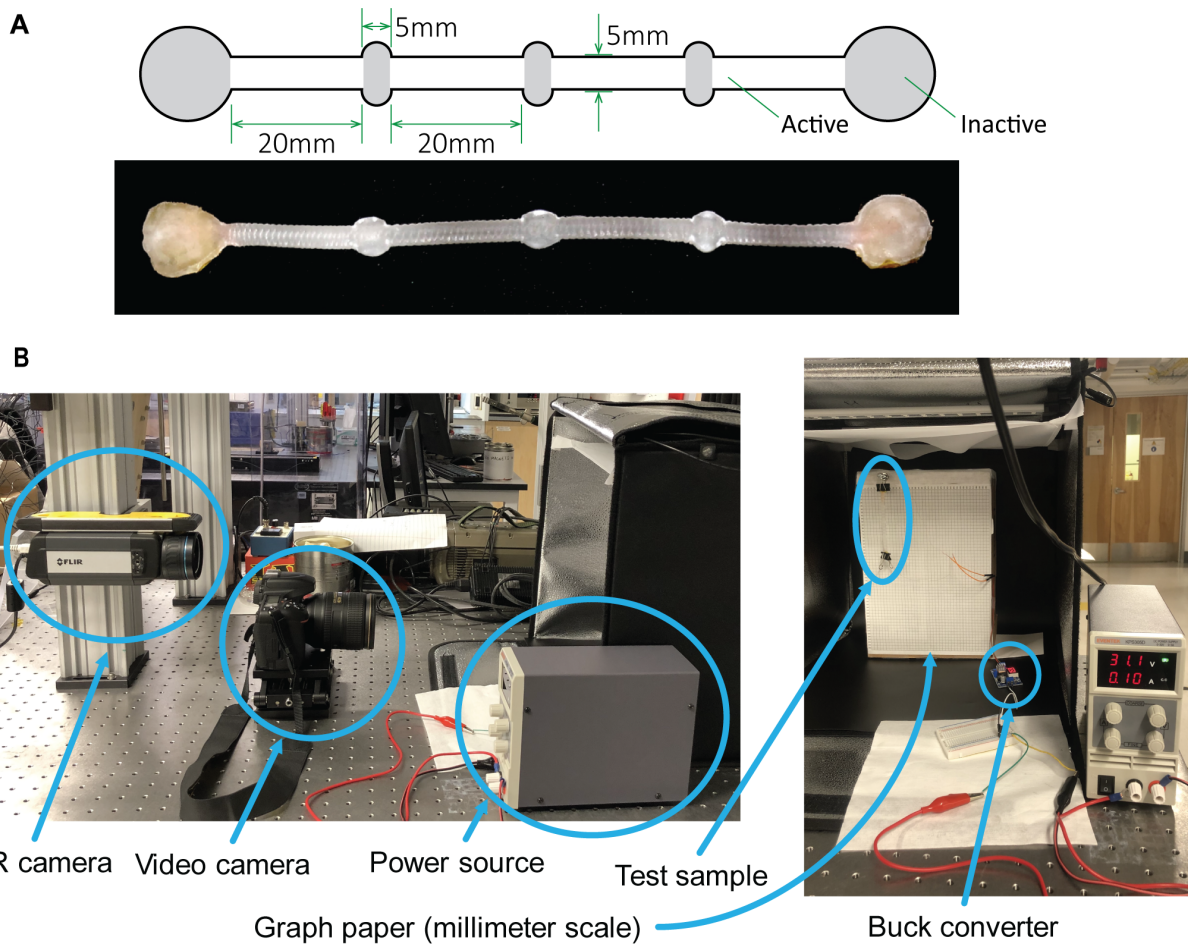


**Fig. S2. Experimental setup for characterization of the actuation behavior of the LCE strips.** (A) Geometry of each individual LCE strip sample in isotropic phase, which is the same as the mold shape. The gray regions are not programmed (i.e., not stretched in the second step of fabrication), so they are inactive to heat stimulus. (B) An infrared camera (FLIR A600) is used to capture the temperature distribution during actuation of the LCE strip. The test sample was placed in front of a graph paper in order to keep track of the amount of contraction with a video camera (Canon). A power source and a buck converter are used to apply the electric current.

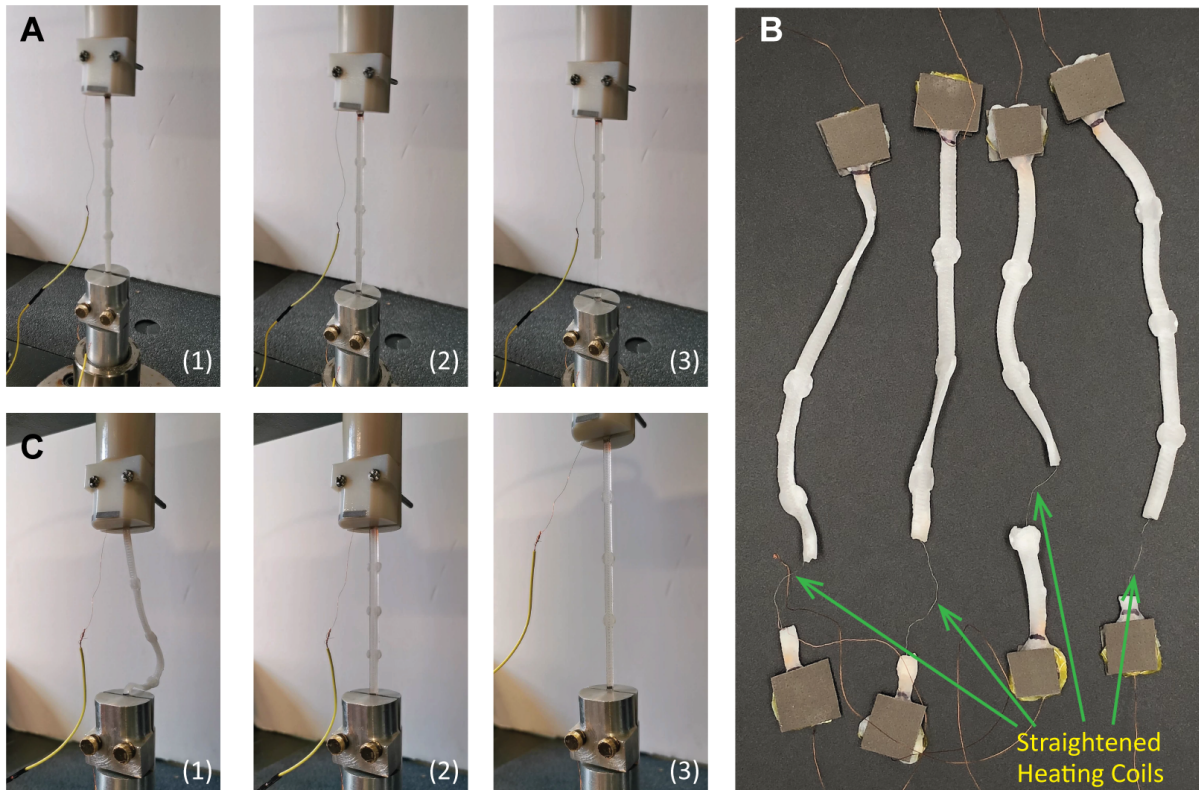


**Fig. S3. Mechanical testing of the LCE strips.** (A) Testing of the actuation force. (1) The LCE strips in their nematic phase are clamped on an Instron 5569 universal testing station (10 N load cell). (2) We apply 0.2 A to heat up the LCE material and actuate its contraction. (3) As the LCE strip contracts, we measure the force asserted on the load cell until the LCE strip breaks. In each experiment, the clearance between the two clamps remain fixed. (B) The broken samples after the actuation force test. The heating coils are stretched but remain intact, even though the LCE strips are fractured. (C) Testing of the stiffness of actuated LCE strips. (1) We first clamp each sample loosely and apply a 0.2 A current. (2) Once fully actuated, the LCE strip becomes straight, and we reduce the current to 0.1 A. (3) We then apply a displacement, to stretch the actuated LCE strip, and record its resistant force.

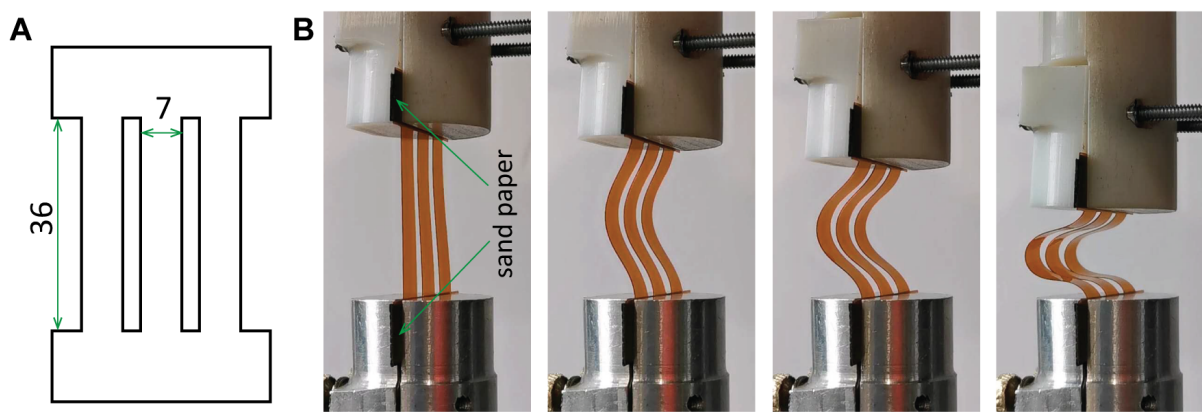


**Fig. S4. Characterization of the buckling and post-buckling behavior of the passive ribbons.** (A) Geometry of each testing sample, which consists of three passive ribbon segments. (B) Snapshots from the testing, showing the buckled shapes of the passive ribbons at different amount of compression. We glue sand papers to the ends of the samples to avoid slipping at fixtures.

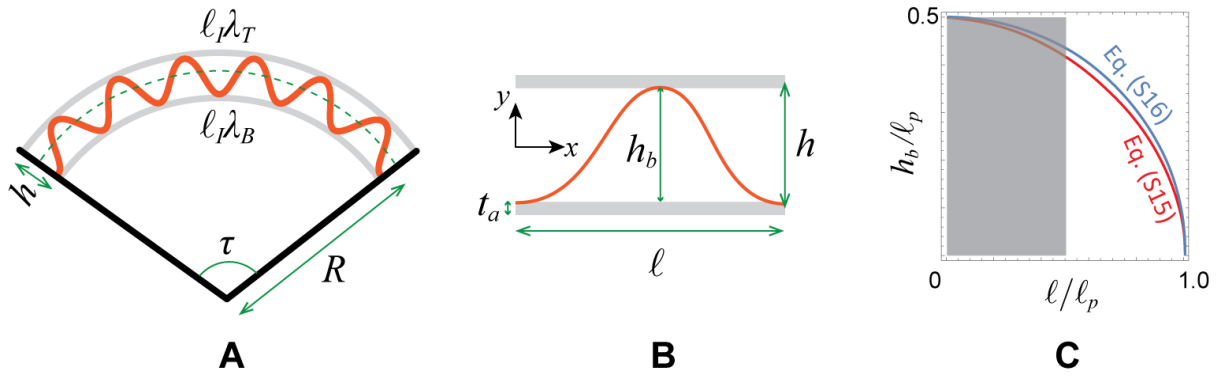


**Fig. S5. Derivation of the curvature of the composite beams.** (A) The curved shape of a composite beam, assuming a perfectly circular shape. (B) The buckled (or actuated) shape of one section of the composite beam. We denote the effective thickness as  $h$ , thickness of the LCE strips as  $t_a$ , the length of the LCE strip in the isotropic phase as  $\ell_I$ , the straight (pre-buckled) length the passive ribbon as  $\ell_p$ , the contracted length of the LCE strips as  $\ell$  ( $\ell_I \leq \ell \leq \ell_p$ ), the buckled height of the passive ribbons as  $h_b$ . (C) Comparison between Eq. (S15) and Eq. (S16). The red curve is a level set of Eq. (S15), given different values of  $h_b$  and  $\ell$ . The blue curve is computed using Eq. (S16), assuming same  $\ell_p$  as the red curve, but given only  $\ell$ .

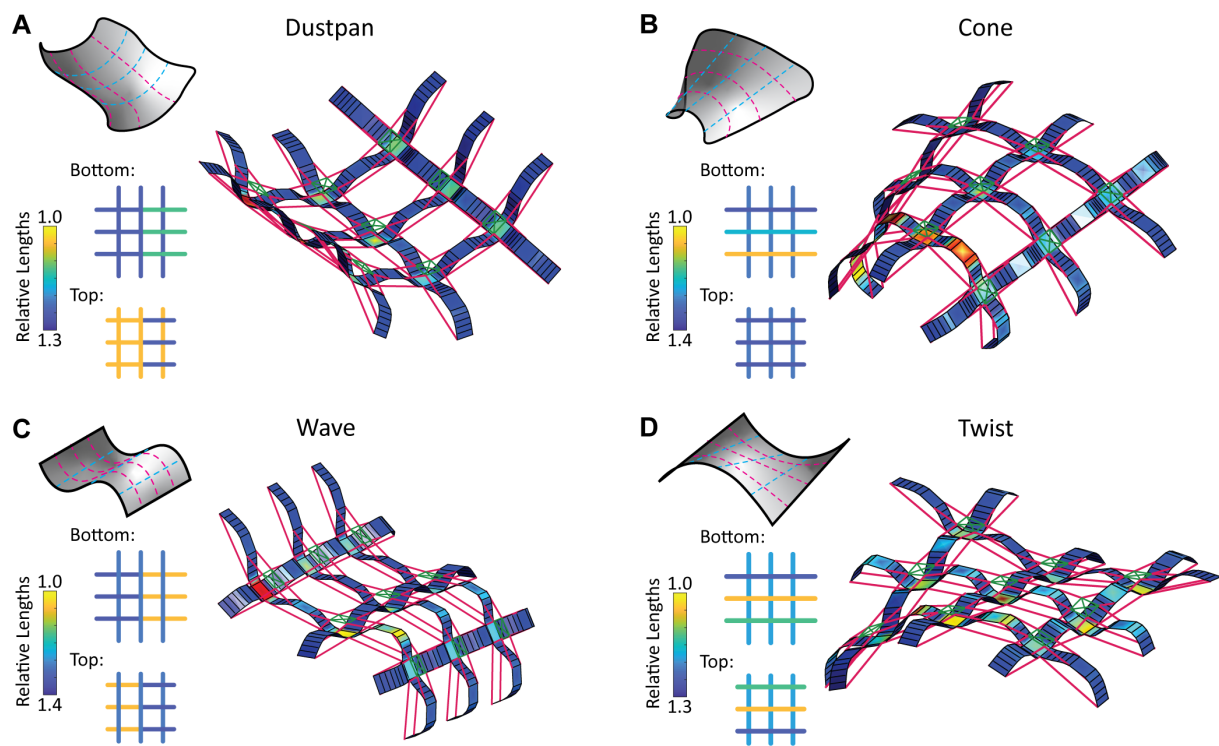


**Fig. S6. Numerical demonstration of geometries obtained by controlling each LCE segment independently.** (A) A “dustpan” shape, which allows the ball to be released from a determined side. The relative length of each LCE segment in the top and bottom grids are shown on the left insets. (B) A cone shape. (C) A wave shape. (D) A twisted (ruled) surface by interpolating between two oppositely bend curves.

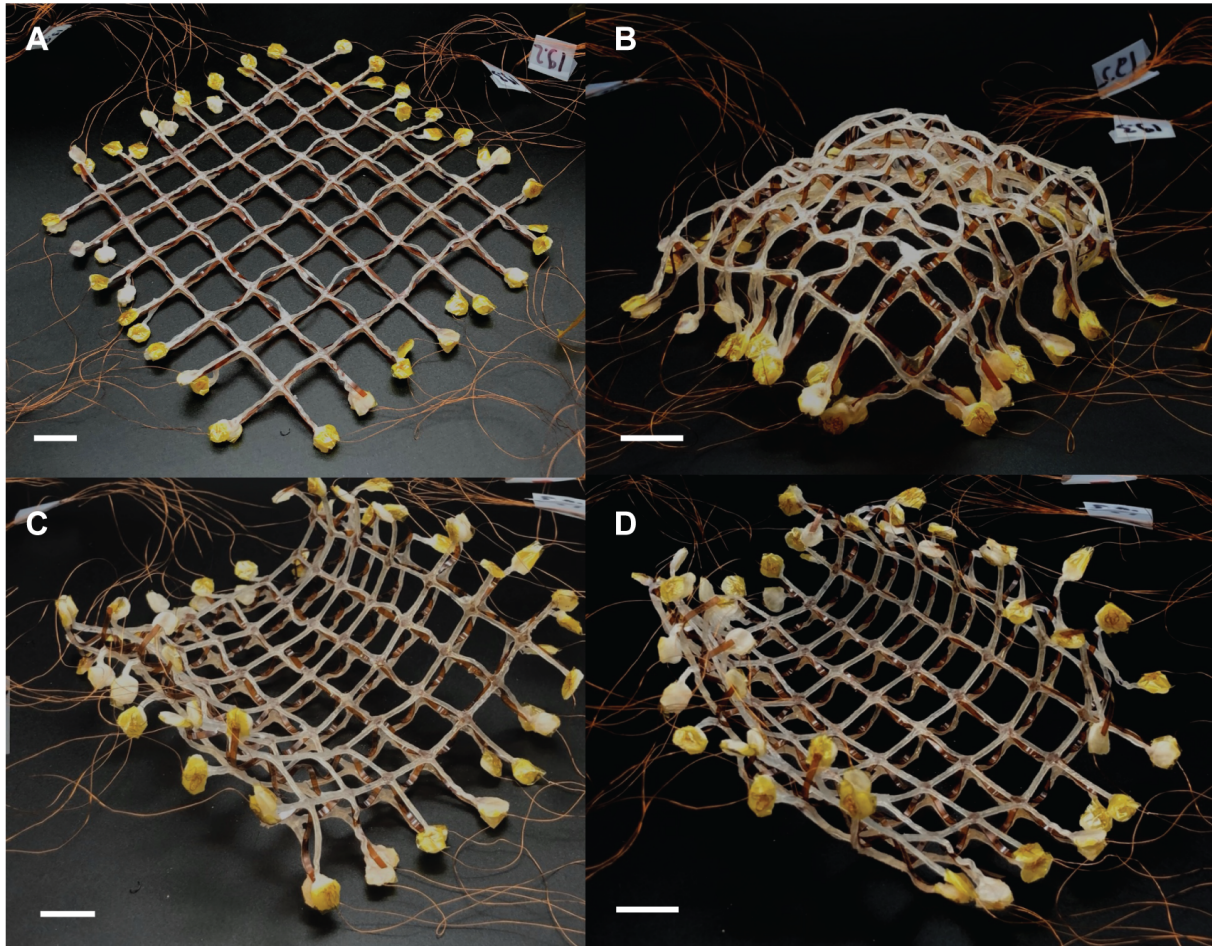


**Fig. S7. A robotic surface with denser mesh grid transforms into various shapes.** (A) The flat configuration before actuation. (B) The dome configuration. (C) The saddle configuration. (D) The cylinder configuration. This robotic surface has 4 control channels laid out similarly to the example shown in the main text (see Fig. 4). We note that the current manual fabrication process is imperfect and manufacturing inaccuracies have significant influence on the final geometries. Other automated technologies, such as 3D printing of LCE (24), may be more appropriate for fabricating robotic surfaces with dense grid meshes.

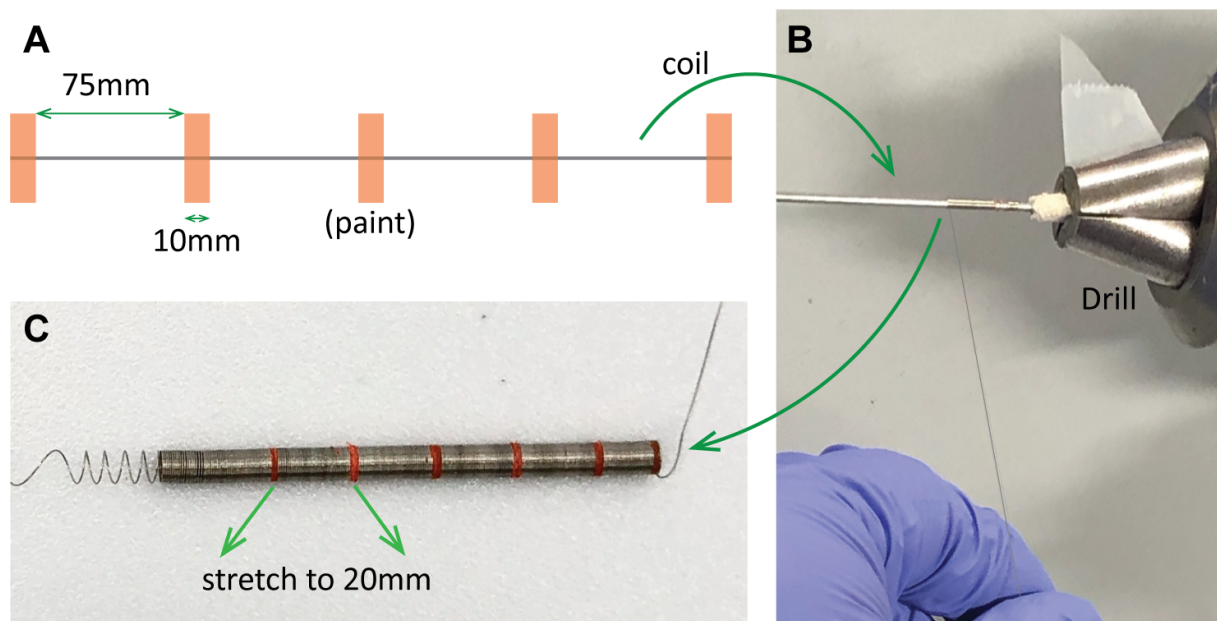


**Fig. S8. Fabrication of the heating coils.** (A) The Nichrome wire is painted to sections of 75 mm in order to ensure same resistance of  $25 \Omega$  in each segment of the grid. (B) A drill is used to wind the Nichrome wires tightly into a coil around a 1 mm-diameter steel rod. (C) Each tightly wended coil is stretched such that each section becomes 20 mm long before being placed into the mold (see Fig. 1).

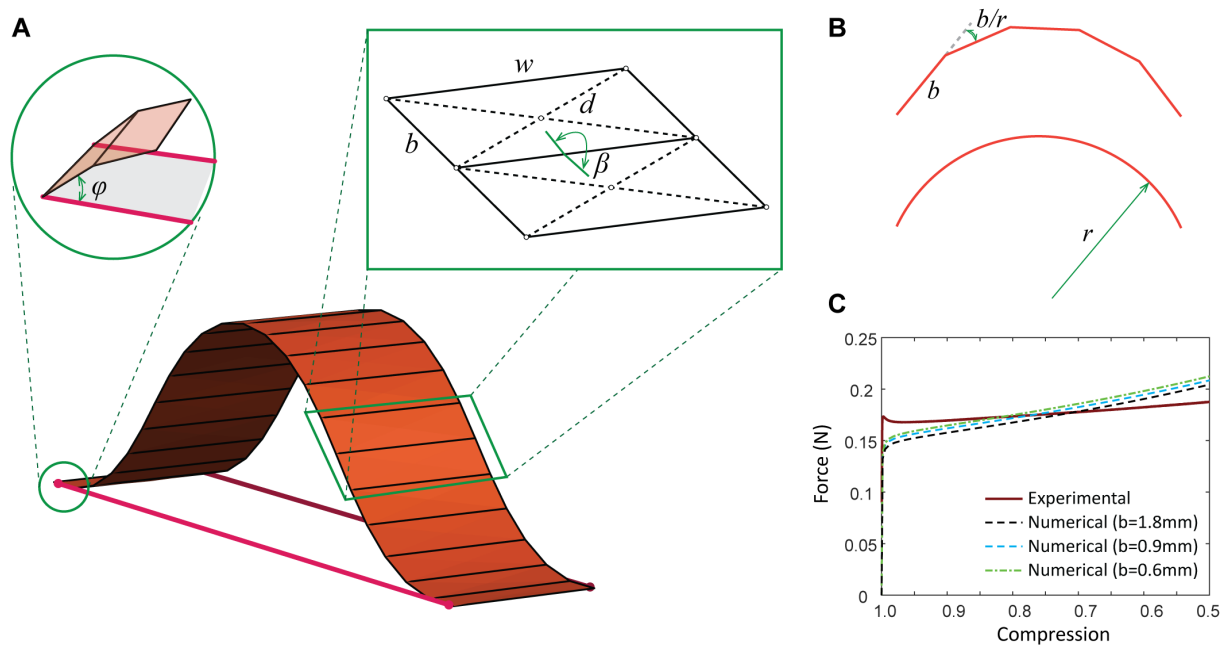


**Fig. S9. The reduced-order model for simplified simulation the robotic surface. (A)** Schematic of the reduced-order model. **(B)** Derivation of the rotational stiffness  $K$  of each torsional spring. The top figure shows the discrete beam, and the bottom figure shows the continuum beam. **(C)** Comparison of the buckling behavior of a passive ribbon between numerical and experimental results. The experimental curve is the average response obtained from 9 tested ribbons. The different numerical results are obtained with different discretization refinements of the ribbon ( $b$  is the edge length, as in Fig. S9A).